CHAPTER 7

On the Geometrical Distribution of Circumnuclear Hydroxyl

THE unification of active galaxies postulates the existence of a circumnuclear torus or a thick disk in order to explain the various emission properties seen toward their nuclear region. In this unification scheme the different orientation of the dusty torus then accounts for the characteristic line emission seen in such nuclei. The specific properties of such a dusty structure depend on the geometry and the dust properties blocking most of the nuclear emission in the optical and infrared bands. In the radio regime this dusty environment becomes almost transparent, allowing a unique view onto the nuclear power plant and its molecular environment. The clear association of the OH emission in the radio and the infrared emission of such galaxies indicates that OH is a perfect tracer for such an environment and therefore a model has been developed to investigate the spectral signature of OH maser emissions for different disk and torus geometries.

In order to reproduce the typical line characteristics of extragalactic hydroxyl Megamaser (OH-MM) emission, a Monte-Carlo approach has been used for which various parameters and their influence to the synthesized spectrum have been evaluated. The model indicates that significant changes of the spectral pattern can be associated with cloud size, opening angle, background continuum emission and different kinematics, that will be discussed for a prototype circumnuclear structure of 450 pc in size. Furthermore, the assumption required for determining the optical depth in this model provides strong evidence to the nature of extragalactic hydroxyl emission itself, that most of the extragalactic maser emission can be explained by an unsaturated maser process.

Hans–Rainer Klöckner

IN PREPARATION

7.1 Introduction and Motivation

Galaxies, which are displaying the majority of visible matter in the universe, show emission properties either dominated by their constituent stars or with a significant non-stellar emission process. These active galaxies harbor Active Galactic Nuclei (AGN), the most luminous objects we know and the best markers of the distant reaches of the universe. Understanding both their physical nature and structure and how to use them to measure cosmological distances and time evolution of galaxies belong to the biggest challenges in modern astrophysics.

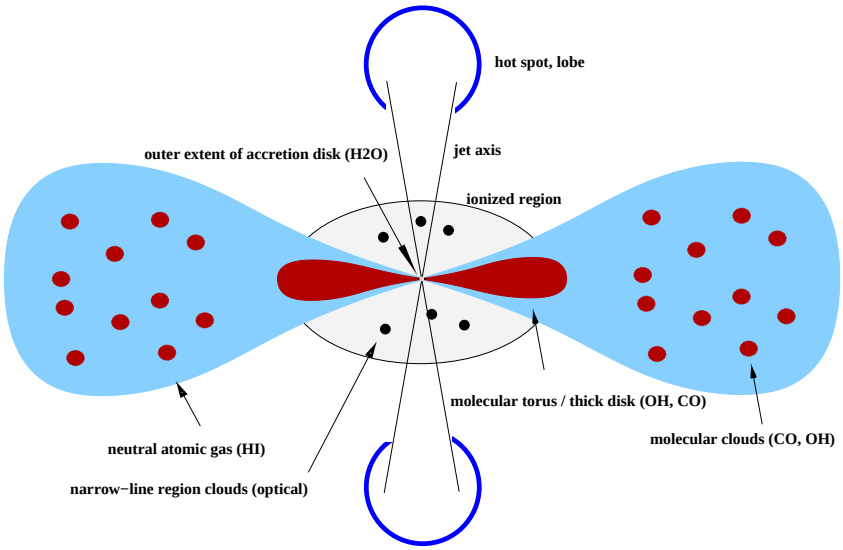

Figure 7.1 – Drawing of the cross section and the hierarchical structure of the inner kilo-parsec region in an active galaxy. The different structures are displayed in schematic size scales and labelled individually by their tracers. In general, the outer tip of the accretion disk is at parsec scales, the molecular thick disk or torus extends up to a few hundreds of parsecs, and the neutral atomic gas together with the molecular clouds is spread in a region of up to a kilo-parsec. The scale size of the outflow can vary from a few parsecs up to several mega-parsecs.

Most of our present knowledge about the three-dimensional structure of the different components in AGN comes from spectroscopic observations of the atomic or the molecular gas phase. AGN, which often out-shine the rest of their host galaxies, are generally accepted to be powered by the release of gravitational energy in a compact accretion disk surrounding a massive black hole (at sub-parsec scale sizes; Rees 1984). Furthermore, the accretion disk is the basis of relativistic, bipolar outflow of material into two symmetric jets sometimes ranging up to a mega-parsec in size. To keep these nuclear engines alive, a constant mass supply is needed from outside the accretion disk. This reservoir of material is thought to be associated

with a nuclear torus or thick disk (see figure 7.1). The resulting non-isotropic distribution of material around the central region is generally believed to be the key in unifying the observed nuclear emission characteristics, within a unification scheme of AGN (Antonucci & Miller 1985; Barthel 1989).

Although the discoveries in two exceptional galaxies, a rapidly-rotating accretion disk in NGC 4258 and an obscuring thick disk or torus in Mrk 231, resulting from observations of extragalactic maser emission, support the scheme of the hierarchical structure of AGN. However, many aspects of their formation, accretion rate, evolution and even the general geometric structure of the obscuring material in such a nuclear region still remain open for debate (Greenhill et al. 1995; Klöckner et al. 2003).

Nevertheless, water-vapor masers are not suitable to study the geometric structure of the obscuring material because the inferred geometry and thickness of the traced disks cannot account for the observed obscuration signature and the radiation patterns seen toward their active nuclei (Maloney 2002; Herrnstein et al. 1998b). Instead the hydroxyl maser features are spread in the inner nuclear region and are located up to a few hundreds of parsecs from the central source (Diamond et al. 1999; Lonsdale et al. 1998; Pihlström et al. 2001). Furthermore, the tight correlation of the OH emission and the infrared emission that emerge from these galaxies indicates that the OH emission is a perfect tracer of the dusty environment in these structures (see chapter 3 and Baan 1989). Therefore, investigating the low spatial resolution spectra of OH Megamaser galaxies may reveal the general properties of the dusty circumnuclear geometry and observations at high spatial resolution may provide important keys to the distribution of blocking material in individual active galactic nuclei (Klöckner et al. 2003; Krolik & Begelman 1988; Krolik 1999, and see chapter 5).

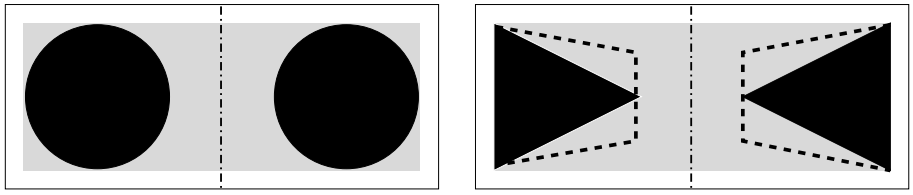

Figure 7.2 – Cross-section of the different geometric structures studied. Left panel displays the torus geometry and the right panel shows the disk and the truncated disk geometry (dashed lines). The vertical lines (dashed-pointed) indicate the symmetry center of each geometry. The half-obscuration angle is determined between the tangential point at the inner edge of the torus geometry and the center of each structure. In order to compare the different geometries, the specific tangential point of the torus geometry determine the height of the inner edge in the truncated disk geometry. Furthermore, the base-length of the disk geometry is determined by the diameter of the torus tube.

7.2 The Method

The method to calculate the spatial distribution and the resulting emission line spectrum is primarily based to best suit the observed properties of maser emission, but it does not strongly restrict this model to such special kinds of emission processes. In order to understand the various line signatures seen in the spectrum of OH Megamaser sources (see figure 7.4), the geometric structure of the circumnuclear environment at three different cross-sections has

been evaluated (for the individual cross-section see figure 7.2). Such a study has been made so far only for a truncated disk geometry in order to explain observations made in the infrared bands of active galaxies. The main result of these studies is that the infrared spectral-energy-distribution (SED) of a dusty disk is much broader than a single black body (Pier & Krolik 1992). In order to explain these infrared observations best, the dusty environment in these models is related to a more clumpy medium rather than a dispersed or solid medium (Nenkova et al. 2002).

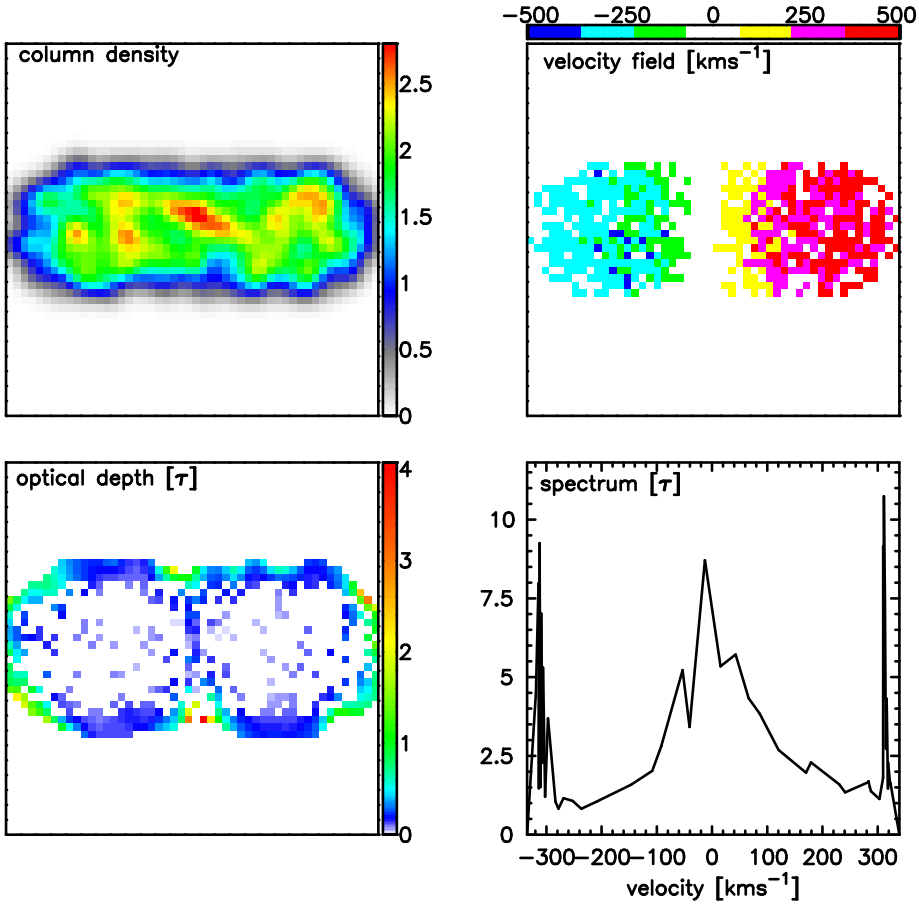

Figure 7.3 – Example of the torus geometry seen edge-on. The individual panels showing the line-of-sight (perpendicular to the plane of the book), column density, the velocity, the optical depth and the expected spectral signature. The model parameters have been set to a maximal extent of 450 pc for the geometric structure, a central mass of 5×10^9 $M_\odot$ with a Keplerian velocity field and a half-obscuration angle of 34°. The quantities simulated here have been determined on the basis of ∼1300 randomly distributed clouds with a Gaussian shaped extent of 2 σ = 24 pc.

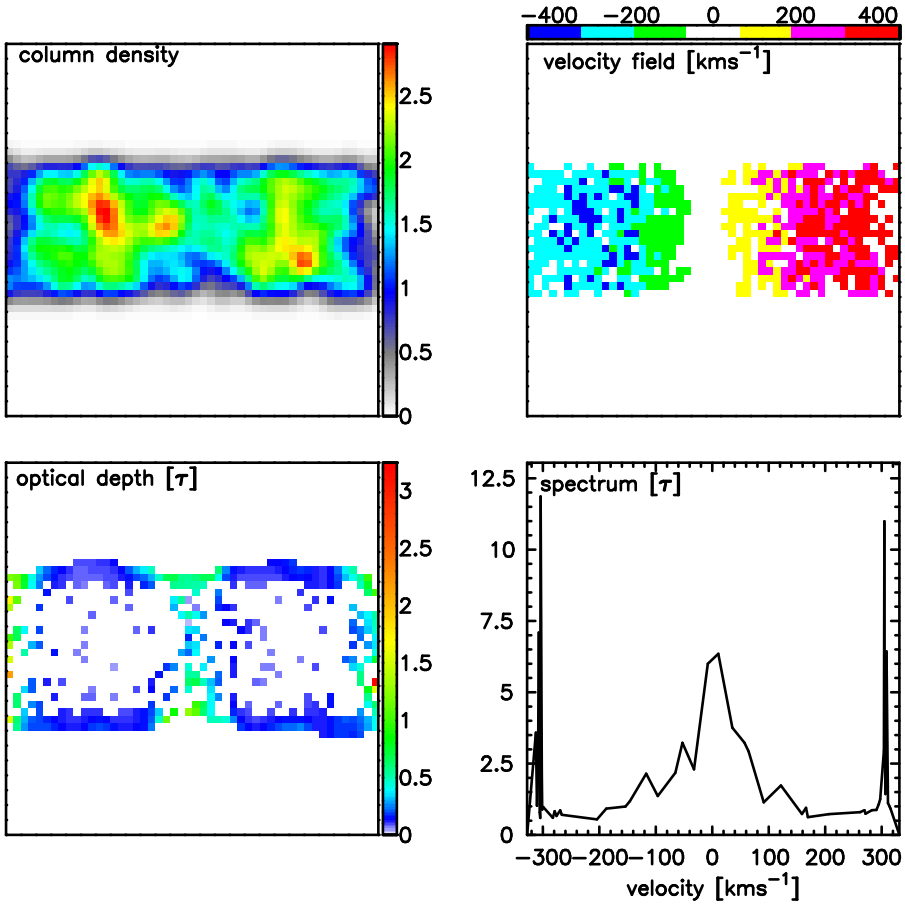

Figure 7.3 – continued; The truncated disk geometry with model parameters and opening angle identical to those of the torus geometry.

For the OH Megamaser emission a strong correlation with the infrared properties of the host galaxy or the nuclear emission has been found and hence it is most likely that the OH emission may trace such a clumpy medium. Therefore, the calculation to describe the spectral characteristics of OH Megamaser emission is based on individual test particles or gas clouds randomly distributed in the 3-dimensional structures of a torus, a truncated disk, and a disk geometry.

Furthermore, based on the general characteristics of OH Megamaser emission that in most cases show little effect of saturation (e.g see chapter 3), the modelled maser emission is assumed to be unsaturated. In the unsaturated limit, where the maser radiation does not influence the molecular populations, the observed line emission emerges from an isothermal medium in the Rayleigh-Jeans regime ($k\,T >> h\,\nu$) and can be described as

$$\mathrm{T_{line}} = [2\,\mathrm{T_s} - 2\,\mathrm{T_{2.7}} - \mathrm{T_{cont}}]\,(1 - \mathrm{e}^{-\tau(\mathrm{v})}), \tag{7.1}$$

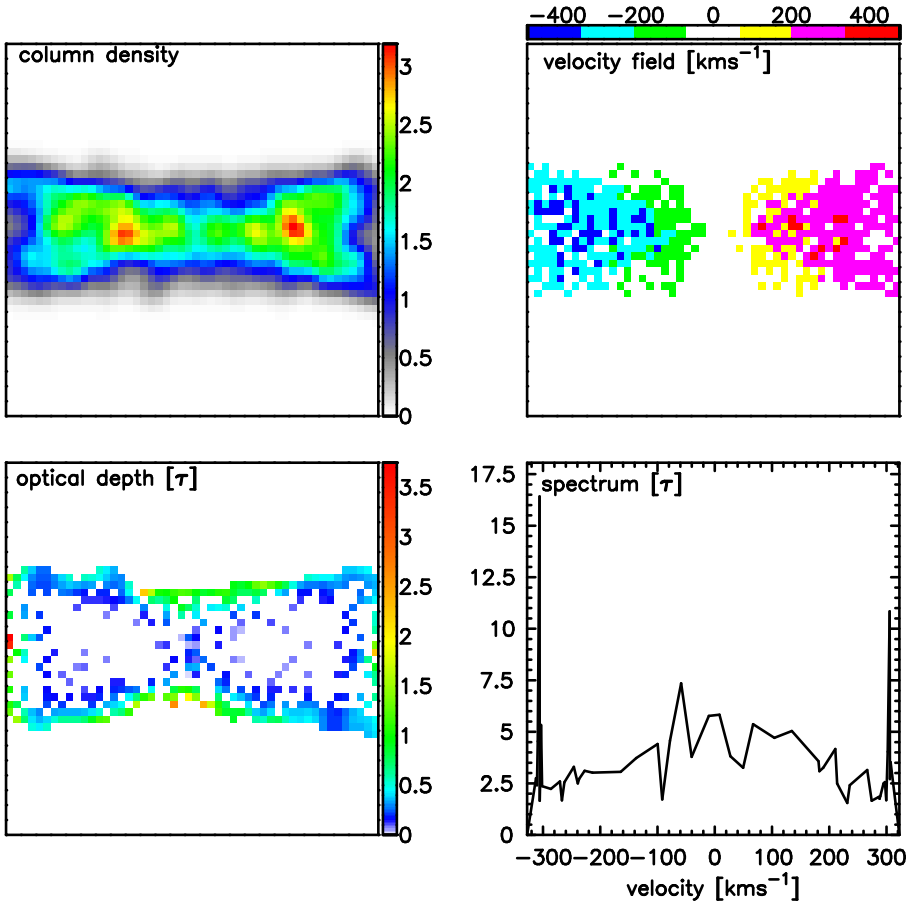

Figure 7.3 – continued; showing the disk geometry with identical model parameters.

where T_s is the spin or excitation temperature, $T_{2.7}$ is the background temperature and T_{cont} accounts for the radio continuum background (Goss 1968). If the continuum emission and line emission do not emerge from the same region, the variation of the optical depth results in different covering factors, which are assumed to be equal. Therefore the optical depth of the unsaturated maser emission line can be described in principle by the absorption coefficient of a two level system, where the energetic higher level is always overpopulated. The line-of-sight (LOS) optical depth can be described by the integration of the absorption coefficient

$$\tau(v,s) = \int\int \frac{h\nu}{c} N_j B_{ji} \left(1 - \frac{g_j N_i}{g_i N_j}\right) \left(\frac{\exp(-\frac{v^2}{2\sigma^2})}{\sqrt{2\pi}\sigma}\right) \times ds\, dv. \tag{7.2}$$

Here the optical depth depends on the column densities, the Einstein coefficient B, the statistical weights of both levels and a Gaussian shaped velocity distribution of each line transition. Now in order to describe the amplification pattern observed in the evaluated geometries, the

column density, the velocity dispersion and the velocity need to be calculated. To do so the calculation is based on the assumption that the numbers of maser photons are directly related to the number of test particles or gas clouds. Furthermore, the maser emission that emerges from randomly distributed clouds is assumed to be emitted isotropically. This assumption is based on the traditional way maser luminosities are given. The isotropic value is $4\pi D^2 F$, where D is the source distance and F the line flux. Since maser emission is highly anisotropic, this can overestimate the true luminosity of an observed maser feature. Nevertheless, precisely because of the anisotropy, there are almost certainly many maser features that are not beamed towards the observers direction, and so the isotropic luminosity based on the observed features may provide a reasonable estimate of the actual maser luminosity (Maloney 2002). Furthermore, in the calculations the space between the individual test clouds toward the center and toward the observer is assumed to be transparent for the individual maser photons. The required velocity dispersion has been determined via the line-of-sight velocity field that can be set to Keplerian or solid body kinematics, where a point-like mass of the individual test clouds or particles in a central potential is assumed. The maser emission or the line-of-sight optical depth in this model are then determined by the column of clouds. The velocity and the velocity dispersion are being estimated in cells of equal width and can be described by

$$\tau_{\square} \sim -\mathrm{N}_{\square} \times \frac{\exp(-\frac{\mathrm{v}_{\square}^2}{2\,\sigma_{\square}^2})}{\sigma_{\square}}, \tag{7.3}$$

where $\mathrm{v}_{\square}$ accounts for the mean velocity in the particular square cell $\square$. This method allows one to determine the optical depth for different geometries, kinematics, and various inclinations. Figure 7.3 displays the LOS column density and the velocity field that are necessary to calculate the optical depth based on equation 7.3.

In general, only a few OH Megamaser galaxies have been observed at spatial resolutions that are high enough to compare the quantities simulated here with the individual characteristics of the masering regions. In the case where the spatial resolution is not efficient enough, the integrated spectrum may be used instead. The model calculation of the integrated spectrum has been performed by averaging over the entire structure. Hereby the direct comparison of the simulated line spectrum with the observed spectrum seen in OH-MM galaxies may be done on the basis of equation 7.1. However, in order to evaluate the different spectral signatures, it is efficient enough to investigate the calculated optical depth. So far, the described model accounts for maser emissions emerging from individual clouds where the maser photons have been produced by self-stimulation.

But the classical OH Megamaser model postulated that sufficient radio background emission may be needed in order to produce such emission (Baan 1989, 1985). In order to determine if such emission is essential for OH Megamasers the emission needs to be investigated on an individual basis. Nevertheless, the effect of such background emission would in general enhance the maser photon rate from each individual cloud and may change the spectral signature. Therefore, the following approach has been realized to simulate the influence of such continuum emission in the model developed. The line-of-sight column density ($\mathrm{N}_{\square}$) is enhanced to account for higher maser emissivity of the individual clouds that are located at sight lines at which background emission is present. In the following the model has been used to produce an overview of various parameters influencing the optical depth and the synthesized

spectrum.

7.3 Evaluation of Various Parameters

In OH Megamaser galaxies the maser emission shows various kinds of spectral signatures that vary from single line features of a few tens of $\mathrm{km\,s^{-1}}$ in width up to multiple line features covering a velocity range of thousands of $\mathrm{km\,s^{-1}}$. At highest spatial and spectral resolutions, the maser emission that shows very broad line emission breaks into several line components revealing the typical spectral characteristics of a single, a double, or a triple line feature. In general, the model developed is capable of producing such spectral features, but in order to provide clues to the geometric setup of the molecular environment in Megamaser galaxies, the observed morphology of the maser emission needs to be evaluated on an individual basis and will therefore be postponed for future investigation. The integrated OH emission spectrum of individual OH Megamaser galaxies shows distinct spectral patterns and therefore is suitable to investigate the general distribution of masering clouds in the circumnuclear region (see figure 7.4). Hereby the OH emission is thought to trace a dusty torus or disk-like structure in the circumnuclear region of the host galaxy. As described in the previous section, the optical depth has been determined by maser clouds randomly distributed in a specific geometry and a Monte-Carlo approach has been used in order to reveal the distinct spectral characteristics of OH emission. An averaged spectrum can be synthesized from hundred independent cloud distributions of the different geometrical structures. The physical setup of a prototype OH-Megamaser emitter has been determined from the general properties revealed by the OH-Megamaser sample. The sample galaxies indicate that the OH emitter shows a mean infrared extent on the order of 450 pc and an averaged line width of 171 $\mathrm{km\,s^{-1}}$ (FWHM), that accounts for a total velocity coverage of about 660 $\mathrm{km\,s^{-1}}$ (see chapter 3). In order to model the specific velocity coverage, the mass of the central source or black hole has been determined to either $(5 \pm 0.5)\times10^9$ $M_\odot$ for a geometry seen edge-on with Keplerian motion or to $(2 \pm 0.2)\times10^9$ $M_\odot$ for solid body motion. To evaluate the model the averaged spectrum has been determined for each geometry for various specifications, such as cloud sizes, obscuration- or opening-angles, changing inclination or line-of-sights, underlying background continuum emission, and different kinematics and will be discussed in the following sections.

7.3.1 Various Clouds Sizes

The OH Megamaser emissions at the lowest spectral resolution show line emission features sometimes spread over thousands of $\mathrm{km\,s^{-1}}$ in velocity, where at higher spectral resolution these emission lines break into individual line features. Nevertheless, the OH Megamaser spectrum generally shows rather smooth emission line features as compared with extragalactic water-vapor emission (see figure 7.4 and chapter 1). This already provides the first characteristics of the individual maser clouds. In order to synthesize a line spectrum with smooth emission lines, each of the individual OH clouds or test particles needs to be extended. To generate the various cloud sizes in the model, the cell sizes of each sight line are variable and can be additionally smoothed by a Gaussian-shaped function.

The influence of the various cloud sizes on the spectral pattern is shown in figure 7.5. Here the spectra indicate that for small cloud sizes the emitted spectrum shows spiky line emission

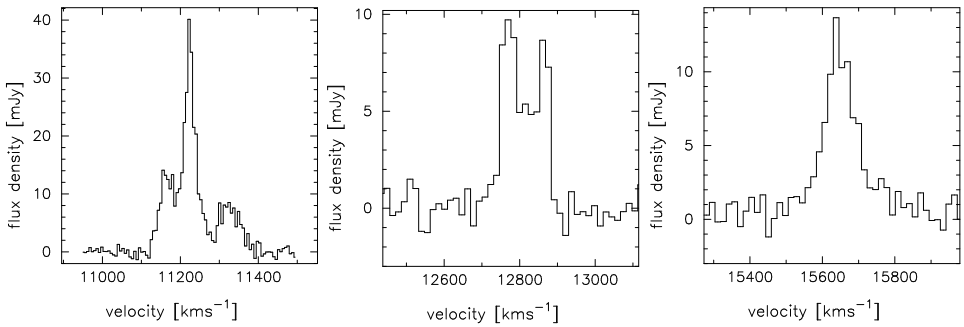

Figure 7.4 – Representative spectra of the extragalactic OH 1667 MHz main-line emission. Left panel: a triple emission line spectrum seen at parsec scale resolution in Mrk 273, such characteristics of triple line features have also been seen toward other Megamaser sources (e.g. IRAS 10039−3338 or IRAS 21272+2514, Killeen et al. 1996; Darling & Giovanelli 2000). Middle panel: double peak line emission seen in IRAS 03260−1422 (chapter 2). Right panel: single emission line feature seen in IRAS 08071+0509 (chapter 2).

features that are broadened by increasing cloud sizes. Note that in the synthesized spectrum the spiky line emission and the large errors at specific velocities are caused by regions of low density with a large variation of the velocity dispersion and the column densities. In general, a smooth spectrum can be achieved for clouds over an extent of larger than 14 parsec (see figure 7.5). In order to reduce the effect of large errors caused by the low density regions, the cloud size of the following simulations has been set to 24 pc.

For the lower limit of cloud size and for the model parameters, the internal velocity dispersion of these clouds is of the order of 44.7 $\mathrm{km\,s^{-1}}$ or 0.2 MHz (for the model parameters see figure 7.3). To evaluate whether such dispersion displays normal conditions in the interstellar medium, the line width can be used to determine the temperature of a stationary layer of gas via $\sigma = 2(\nu/\mathrm{c})\sqrt{\frac{\mathrm{kT}}{\mathrm{m}}}$, where m is the mass of the hydroxyl molecule ($\mathrm{m_{OH}}$ = 0.984 amu = 1.66 10^{-27} kg and for further astrophysical quantities see Cox 2000; Cook 1977). To describe the synthesized dispersion of the clouds, such a gas layer must have a temperature on the order of 5.5×10^4 K. Such a high temperature has been seen in the hot ionized gas phase in the ISM that is thought to be produced by supernova explosions (see e.g. Walter 1999). Therefore the high velocity dispersion most likely indicates turbulence seen in the dusty environment rather than physical gas temperatures. This result is quite striking, because maser emission is expected to show low dispersion in order to conserve velocity coherence for the individual maser photons and provides an additional clue on the maser process itself. Such velocity dispersion would account for optically thin conditions for the infrared pumping lines and therefore for a continuous pumping mechanism.

7.3.2 Various Obscuration Angles

The influence of the various obscuration angles of the individual geometrical structures on the averaged spectrum of the maser emission is shown in figure 7.6. The displayed spectra are shown for an edge-on geometry at which the largest systematic changes in the averaged spectrum are expected. In principle, only the torus and the truncated disk geometry have identical

obscuration angles, because of systematic errors in determining the obscuring angle for the disk geometry. This error is caused by the fixed spatial extent of the masering structure, but it is well understood and grows for an increasing obscuration angle. The determined obscuration angle of the disk geometry will be systematically smaller than for the other geometries. Therefore, the spectra of the disk geometry for high obscuration angles should be taken for reference only. For the different cross-sections and the definition of the opening angle see figure 7.2. Note that the maximal path length of an edge-on disk in this model is defined by the same length of the torus tube. At small obscuration angles where the systematic effect of the disk geometry is rather small, all three different geometries show similar synthesized spectra. In particular, these spectra show triple emission line features with a dominant line emission feature at center velocity. The central line feature in a truncated disk geometry shows a slightly enhanced optical depth with respect to the other geometries, that is related to the larger number of clouds at systemic velocity. In general, for the individual geometries in figure 7.6, the strength of the central line feature with respect to the line features at the edges of the spectrum is decreasing for an increasing obscuration angle. Furthermore, for small obscuration angles the central line feature is slightly narrower than the line features at the edges of the spectrum. However, no clear distinction between the different geometries can be made, although for small obscuration angles the central line emission feature of the truncated disk may indicate a higher optical depth compared with that of the torus geometry.

In order to determine the appropriate obscuration angle for further investigation of the model structure, the obscuration angle can be compared with the opening angle that has been found by the relative number counts of Seyfert type galaxies. The difference between the half-obscuration angle used in the simulation and the half-opening angle is 90°. The most interesting outcome of the evaluation of the obscuration angle is that in order to produce triple line emission features with a stronger central component in a spectrum, the model predicts half-obscuration angles ranging from 50° to 30° (or 60° to 40° half-opening angle). This range covers remarkably the opening angles found for various samples of galactic nuclei (Schmitt et al. 2001, and references therein). The specific opening angle found for these types of galaxies has been shown in figure 7.7. For the half-opening angle of 38° (Seyfert 1 to Seyfert 1.5) the OH emission spectra would show almost equally enhanced emission line features at the edges with respect to the central emission line feature (half-obscuration is 52°, top panel of figure 7.7). Such a specific spectral signature has not been seen in OH-MM galaxies and therefore this opening-angle has been excluded to explain the OH emission. The same is true for the half-opening angle of 48° (Seyfert 1 to Seyfert 2), where the OH emission spectra show almost equal height of the line emission features at the edges and the center velocity of the spectrum (half-obscuration is 42°, middle panel of figure 7.7). Also for a half-opening angle of 56°, which has been seen in a sample of Seyfert 1.8 to Seyfert 1.9 galaxies, a distinct difference in strength of the triple lines could not be clearly determined (half-obscuration is 34°, bottom panel of figure 7.7). Nevertheless, the simulation in figure 7.6 shows that the strength of the central line emission feature increases for smaller obscuration angles and therefore the lowest determined opening angle has been used for the following investigations.

7.3.3 Various Line-of-Sights

The influence of changing line-of-sights (LOS) on the different geometric structures and on the synthesized spectrum is shown in figure 7.8. For increasing inclination, starting from

edge-on (inclination = 0°) to almost face-on (inclination = 90°), each geometry shows strong changes of the averaged spectrum. In general, the velocity range covered by the modelled optical depth decreases for increasing inclination for all geometries. Furthermore, the influence of strong variations of the optical depth is indicated by large errors in the averaged spectrum that increase for higher inclination. Such systematics is caused by specific regions of low density and various velocity dispersion mostly located at the outer boundaries of the individual structures. The most significant change to the averaged spectrum for each geometry is that, for increasing inclination, the specific emission line features at the edges of the spectrum disappear for inclinations larger than $\sim 15^\circ$ and only the central emission line feature remains from the triple line pattern. At increasing inclinations this central emission line feature remains as a broader emission band up to inclinations of about 60°. For inclinations larger than 60° that specific broad emission band vanished to an almost featureless narrow line emission.

Summarizing, for various inclinations no systematic difference can be seen in the averaged spectral pattern for the different geometries.

7.3.4 Influence of Background Emission

The influence of background continuum emission is evaluated and shown in the figures 7.9 and 7.10, where the averaged spectra have been synthesized for continuum emission affecting clouds at specific regions in each of the different geometries. So far, in the presented simulation the assumption has been made that each cloud contributes equally to the synthesized emission line spectrum. In order to simulate the influence of background continuum emission to the maser emission, the emissivity of each cloud has been changed. It has been realized that the maser photon emissivity of such clouds is enhanced by the factor of the square root of the total number of test clouds located in each geometry. By applying this factor, the increase of emitting photons per cloud accounts for the statistical error and does not dominate the individual spectrum in the Monte-Carlo simulation.

In the first approach, the influence of background emission that emerges from the central region has been simulated. For this setup the assumption is made, that the continuum emission affects all clouds in the front side of each geometry towards the observer. Such background emission shows no clear change of the spectral pattern in the spectrum (see top panel in figure 7.10). This result is explained by the symmetry of the distribution of clouds in the back- and front-side of each geometry, where the spectral pattern so synthesized is similar to a spectrum produced by a factor two less clouds. In order to see if background emission is capable to produce significant asymmetries in the averaged spectrum, the influence of continuum emission affecting the cloud emissivity at specific parts of each geometry has been investigated. Hereby, the influence of continuum emission affecting clouds at certain radii is displayed in figure 7.9. Such continuum emission generally influences the strength of the central line with respect to the line features at the edges of the spectrum. Here it is found that different geometries affect the averaged spectrum. For a torus- and disk-like structure the features at the highest velocities are heavily reduced, whereas these line features are relatively enhanced in the truncated disk compared to the central emission line feature. Apart from this result no clear asymmetry in strength or in spectral shape of the line emission features could be produced (for an asymmetric spectrum see e.g. figure 7.4). Another approach to produce asymmetries in the spectral pattern is to have continuum emission that affect only specific sections of the individual geometries. The influence of such background emission has been

displayed in figure 7.10. The definition used for the individual sections at which background emission affects the cloud emissivity is based on a face-on structure. The range between 360° to 180° is defined as 21:00 hrs – 15:00 hrs and a 30° section e.g. at 270°– 240° corresponding to 12:00 hrs – 13:00 hrs. As already described above, there is no influence of background emission to the spectral pattern if clouds are affected in the region between 180° to 360° (top panel figure 7.10). Apart from this, clear evidence is found that individual regions account for specific asymmetries in the spectral signature. Line features at the edges of the spectrum can be enhanced by increasing the emissivity of the particular clouds ranging in the region 180° and 210°, whereas a clear asymmetry of the line features can be achieved by clouds in the region between 210° to 240°. In addition, a asymmetry of the central line feature can be produced by continuum emission affecting the region between 240° to 270°.

Summarizing, asymmetries in an OH emission spectrum can be produced by asymmetries of an underlying continuum emission, where the background continuum emission illuminates only some parts of the foreground maser structure. In reality such asymmetry can be caused by a radio outflow being misaligned to the axis of symmetry of the molecular environment in the circumnuclear region. Evidence that such misalignment is possible in nature is displayed by different orientations of the radio outflow and the maser emission seen in the OH-Megamaser galaxy Mrk 231 (Klöckner et al. 2003).

7.3.5 Radial Velocity Component

The asymmetry of the line shape of individual emission line features in the spectrum of OH Megamaser galaxies may, apart from the underlying continuum emission, also be caused by outflow of material (Baan et al. 1989). The influence of outflow on the velocity would not change the general appearance of the velocity field, but it would influence the orientation of the minor symmetry axis of the velocity field. This can be explained as follows: if outflow is present the line-of-sight velocity [$\mathrm{V_{LOS}}$] is a combination of the circular velocity [$\mathrm{V_c}$] and radial outflow velocity [$\mathrm{V_r}$] described by

$$\mathrm{V_{LOS}}(\phi) = \mathrm{V_0} + \mathrm{V_c}\sin(\phi) + \mathrm{V_r}\cos(\phi), \tag{7.4}$$

where $\mathrm{V_0}$ is the systemic velocity and ϕ describes the angle to the symmetry axis of the major axis of a face-on seen circular geometry. Note that $\mathrm{V_c}$ in this model is determined for Keplerian or solid body kinematics. In particular, to understand the influence of both velocity components ($\mathrm{V_c}$ and $\mathrm{V_r}$), it is helpful to evaluate the special cases at which one of the components is negligible. For a sight line towards the center of an edge-on geometry the radial outflow would dominate the LOS velocity, whereas at the edges the radial component is negligible for the LOS velocity. In principle, outflow only affects the orientation of the minor axis with respect to the major axis of the velocity field and does not change its general appearance. Therefore changes of the velocity field caused by outflow have been realized in the model by rotating the minor axis of the velocity field. In figure 7.11 the influence of radial outflow on the spectral signature is shown by increasing the orientation by factors of 15°. In particular, a change of 15° in azimuth does not show a general change of the spectral signature. But in comparison to ordinary Keplerian kinematics, the central emission feature shows lower amplitude and a broader line width. By increasing the influence of the outflow on the velocity field, the averaged spectrum shows a less enhanced central emission component, that completely vanishes for an outflow that causes a 45° change in the orientation of the minor axis of the velocity field.

7.3.6 Solid Body Kinematics

In order to investigate the effect of different kinematics on the synthesized spectrum, Keplerian and solid body rotation have been evaluated. Intuitively, the solid body rotation may not play a role in extragalactic maser emission, but it has been shown that in some galactic nuclei the motion traced by spectral lines can mimic a solid body rotation (Spoon et al. 2003; Cole et al. 1999). Therefore, the required mass density must in principle increase with larger radii. Such an effect may be achieved by the distribution of massive stars producing an averaged density that mimics solid body rotation.

The principal change to the spectral signature of this type of kinematics at various inclinations is displayed in figure 7.8. Compared to the averaged spectrum of a Keplerian velocity field (e.g. bottom panel figure 7.7), the synthesized spectrum for an edge-on geometry shows a rather smooth spectral pattern, where the central line feature is weaker and shows a broader line width with respect to the features at the edge of the spectrum. For an increasing inclination this specific spectral pattern changes dramatically for the individual geometries. For a torus structure the spectral pattern shows only small changes at inclinations ranging from 90° (edge-on) to 30°. For lower inclinations, the line features at the edge of the torus spectrum disappear for almost face-on sight lines. These line features disappear for the truncated disk structure and the disk structure already for small deviations from an edge-on sight line. Furthermore, the disk geometry shows no clear spectral line feature for increasing inclinations.

Summarizing, for an edge-on seen geometry no specific spectral differences are produced by Keplerian or solid body rotation. Nevertheless, a clear difference between these two types of kinematics is revealed for changing inclinations, and furthermore clear distinctions for the different types of geometries are found.

7.4 Conclusions

The simulations evaluated here are to first order to understand the spectral signature seen in the spectrum of individual OH Megamaser sources. Based on a fixed set of global parameter that had been adopted from the averaged values of the OH Megamaser sample, a prototype emission spectrum has been produced in order to relate principal changes of the distribution of masering clouds and various physical parameter to general changes in the spectral signature.

In general, the simple assumption that optically thin masering clouds are randomly distributed in a certain geometry is capable of reproducing the basic line emission features seen in OH Megamaser galaxies (see figure 7.4). Furthermore, the assumption used to calculate the spectral signature of the emission line spectrum provides another good constraint on the nature of the extragalactic hydroxyl maser emission processes itself. In order to give a rather smooth spectral pattern, the maser clouds need to be extended and show turbulent velocity profiles, that would provide enough line-of-sight velocity that the infrared pumping is not affected by large optical depth. Therefore, the model developed here supports the concept that OH Megamaser emission is produced by an unsaturated maser process.

Furthermore, the model is used to investigate the spectral pattern caused by a different distribution of maser clouds in a nuclear region of maximal 450 pc in extent. This geometry setup is in general capable of explaining the typical OH Megamaser emission signatures of a single, a double, and a triple line emission feature. In order to reproduce a triple line emission feature with an enhanced central line feature in the spectrum, the individual geometries need

to be seen almost edge-on with an obscuration angle ranging between 50° to 30°. A true double line emission feature cannot be produced with the model by changing only general properties. Moreover, to produce such double line emission characteristics, the model indicates that the velocity field needs to be influenced by a radial velocity component possibly produced by outflows. Nevertheless, the model indicates that either for large opening angles, solid body kinematics or large inclinations, the line emission features at the edges of the spectrum can be strongly enhanced with respect to the central emission feature and therefore can mimic a spectrum with double line characteristics. A single line feature can be produced by changing the line-of-sight for the individual geometries. For inclinations lower than 80°, the spectral patterns show a single line emission feature at center velocity for geometries seen almost face-on.

In addition, in some cases OH Megamaser emission shows asymmetries both in the line spectrum as well as in the profile of single emission line features. The model shows that an outflow or radio background emission is necessary to produce such asymmetries. For further investigation of the influence of background emission on the spectral pattern, the structural information of individual OH-Megamaser galaxies needs to be evaluated.

Basically, the motivation to investigate the spectral signature of OH emission has been to produce constraints on the individual geometries of the circumnuclear environment of such galaxies. These investigations shows that no general spectral signature can be associated with a specific geometry. Only slight differences in the spectral signature of individual geometries could be found by applying background continuum emission or different kinematics to the geometric structure. The model developed has also been used to determine general changes to the spectral pattern and has not taken into account the spatial distribution of the OH emission. Therefore, the geometric distribution of the OH emitting clouds may only be investigated by means of individual observations at sufficient spatial resolution, in order to provide a constraint on the geometric structure of the obscuring material in active galaxies.

Acknowledgments

I would like to thank Edo Loenen for advice on programming in Python and Kplot software, and furthermore, the software group and here in particular Maarten Breddels of the Kapteyn Institute for developing Kplot, which is a visualization tool for Python.

7.A The Influence of Various Parameters on the Averaged Spectrum

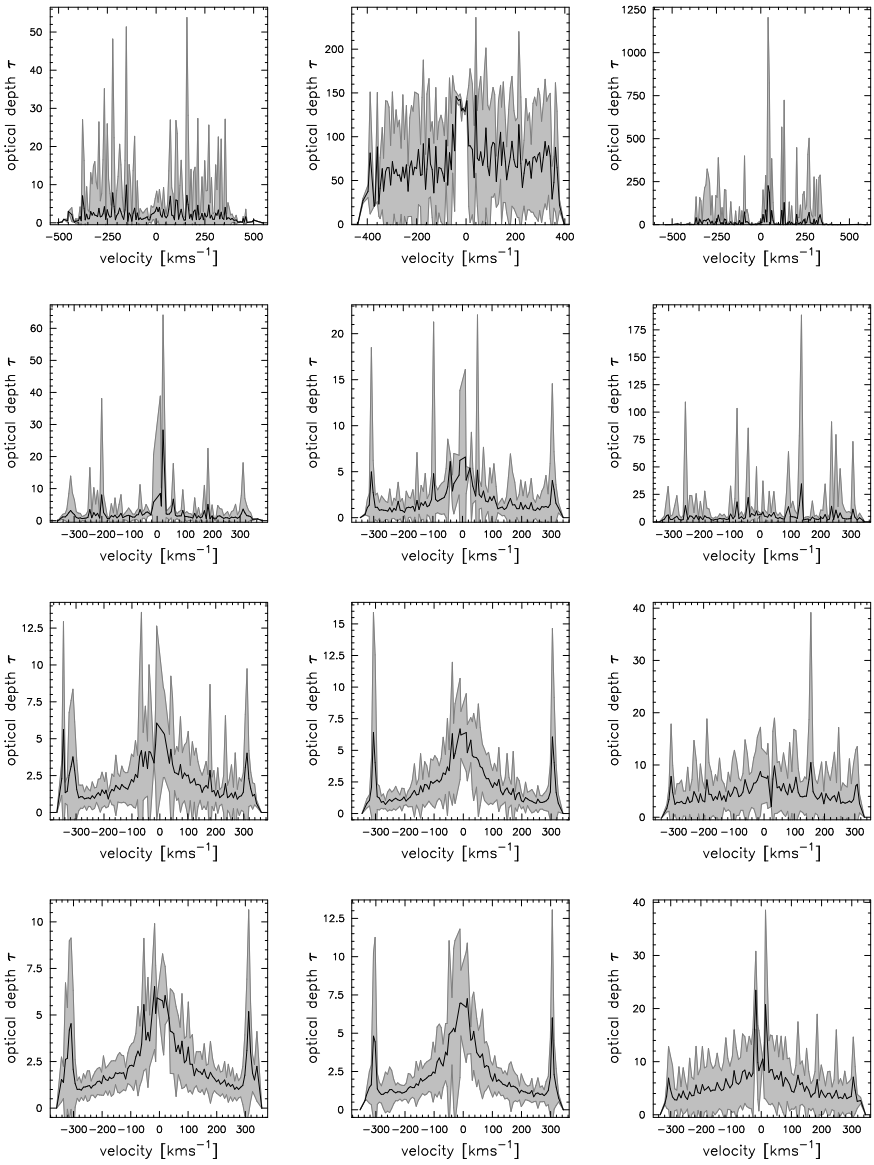

Figure 7.5 – Averaged spectra for different cloud sizes from left to right for an edge-on **torus**, **truncated disk** and **disk**-geometry. From top to bottom the cloud sizes increase. The clouds have a projected Gaussian shape mass distribution of 2 σ in size of 3.5 pc at the top, 9.7 pc, 14 pc and 24 pc at the bottom. Each spectrum has been averaged to a velocity resolution of about 7 km s^{-1} and the estimated error for each velocity bin have been determined by 100 independent cloud distributions and is indicated by the gray frame. The model setup is similar to the parameters described in figure 7.3.

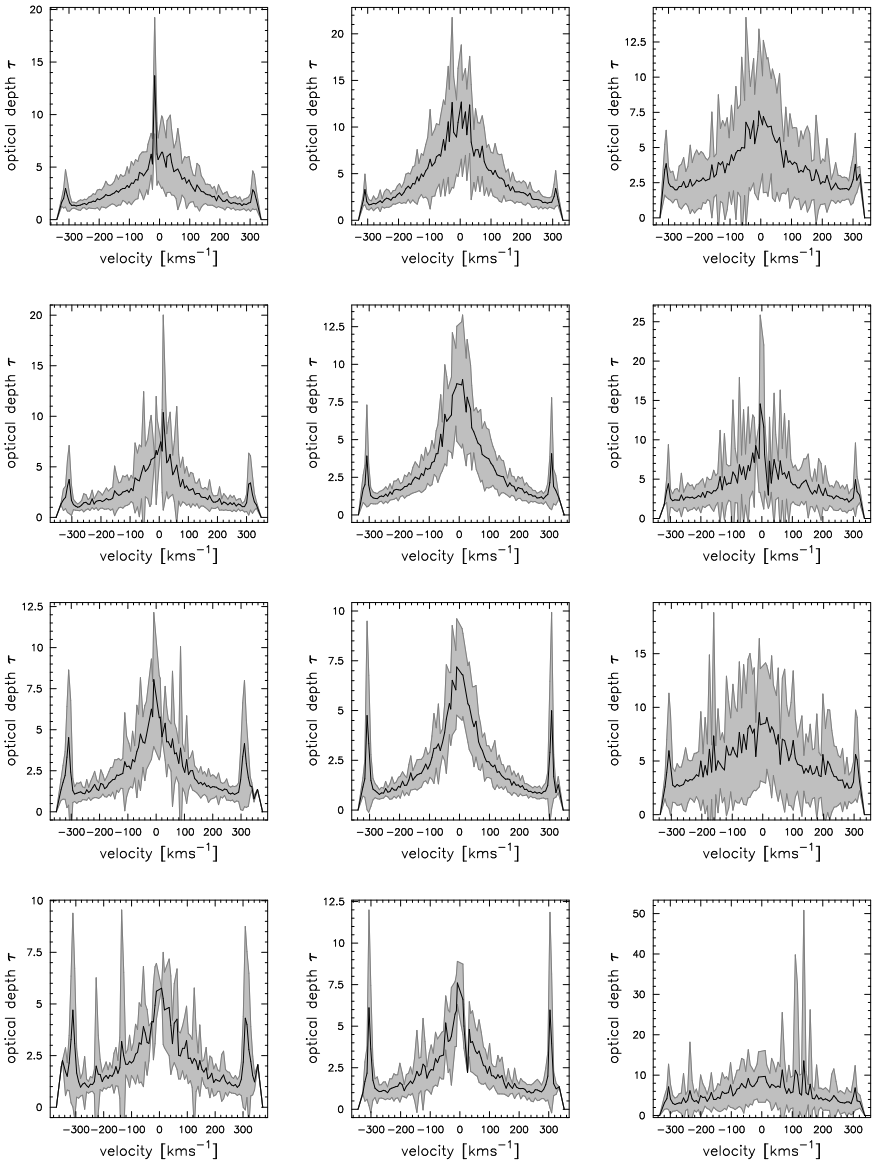

Figure 7.6 – Averaged spectra for different obscuration angle from left to right for an edge-on **torus**, **truncated disk** and **disk**-geometry. From top to bottom the half-obscuration angle increases from 10° in steps of 10° to 40° at the bottom. Each spectrum has been averaged to a velocity resolution of about 7 $\mathrm{km\,s^{-1}}$ and the estimated error for each velocity bin has been determined by 100 independent cloud distributions and is indicated by the gray frame. The model setup is similar to the parameters described in figure 7.3.

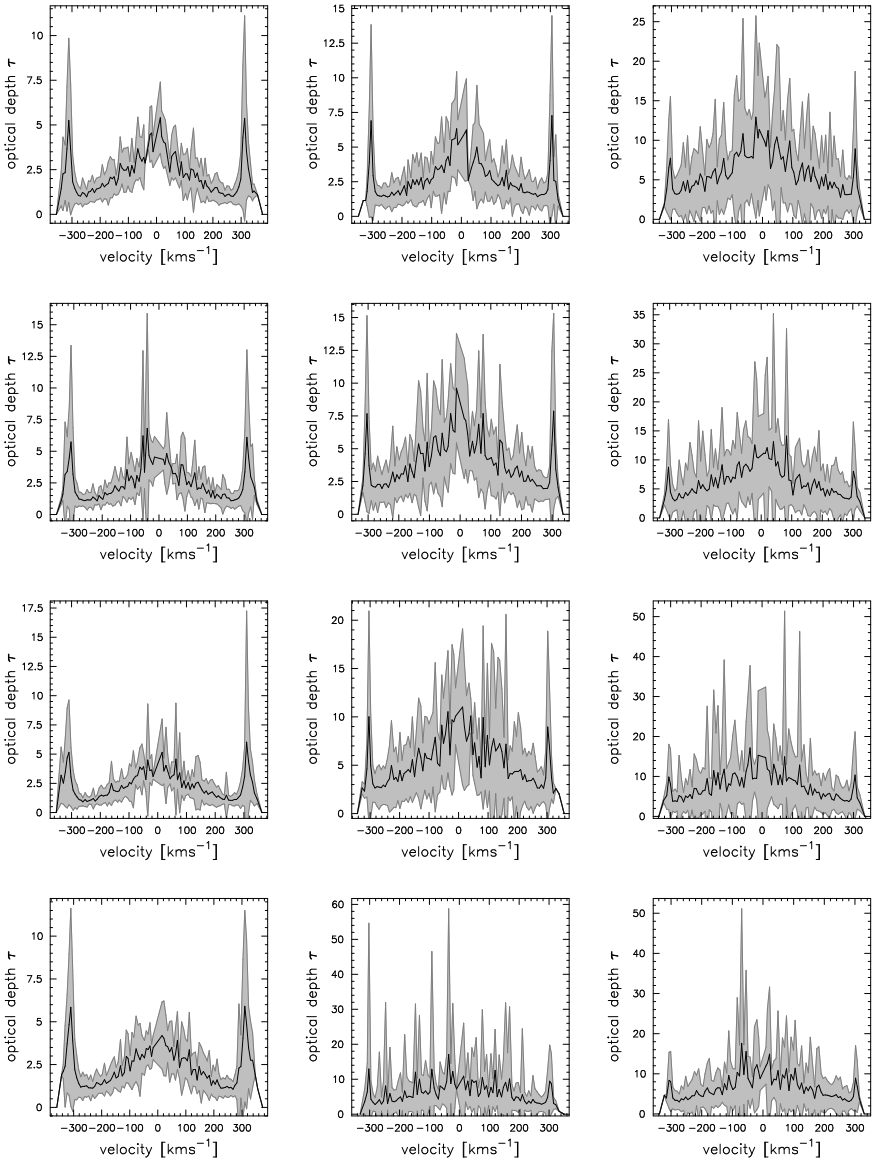

Figure 7.6 – continued; starting at the top with a half-obscuration angle of 50° and increasing in steps of 10° to 80° at the bottom.

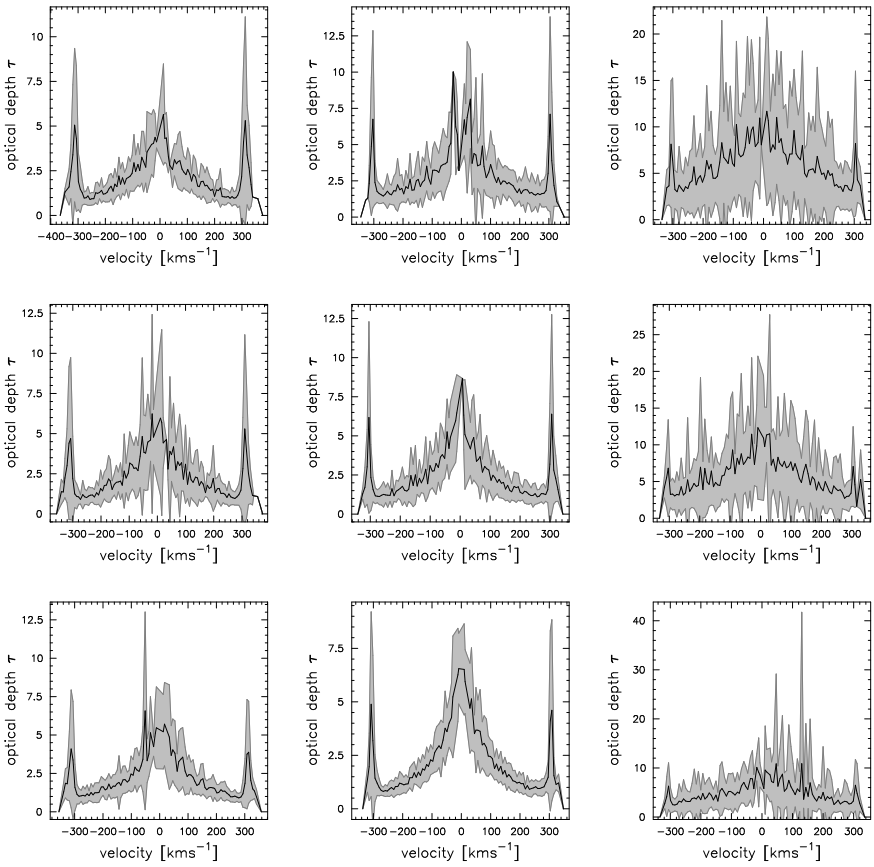

Figure 7.7 – Averaged spectra for specific obscuration angle found for relative numbers of Seyfert nuclei. The spectra from left to right are determined for an edge-on **torus**, **truncated disk** and **disk**-geometry. The half-obscuration angle at the top of 52° accounts for a half-opening angle deduced from the relative numbers of Seyfert 1 to 1.5 types; in the middle panel the obscuration angle of 42° for Seyfert 1 to 2 and 34° for Seyfert 1.8 to 1.9 types at the bottom (Schmitt et al. 2001). The model parameters are similar to the setup described in figure 7.3. Each spectrum has a velocity resolution of about 7 $\mathrm{km\,s^{-1}}$ and the estimated error for each velocity bin is determined by 100 independent distribution of the maser clouds in the specific geometry and is indicated by the gray frame.

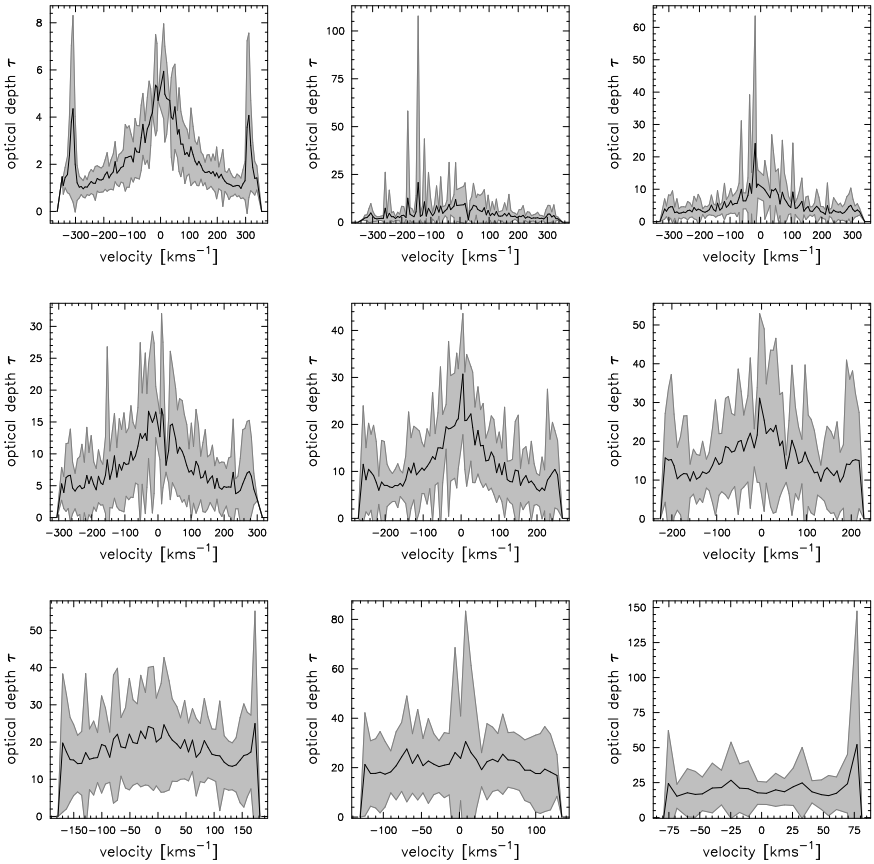

Figure 7.8 — Averaged spectra for a **torus** geometry seen at different inclinations. From the top left to the bottom right the inclination decreases by a step of 10 degrees. The model parameters are similar to the setup described in figure 7.3. Each spectrum has a velocity resolution of about 7 $\mathrm{km\,s^{-1}}$ and the estimated error for each velocity bin is determined by 100 independent distribution of the maser clouds in the specific geometry and is indicated by the gray frame.

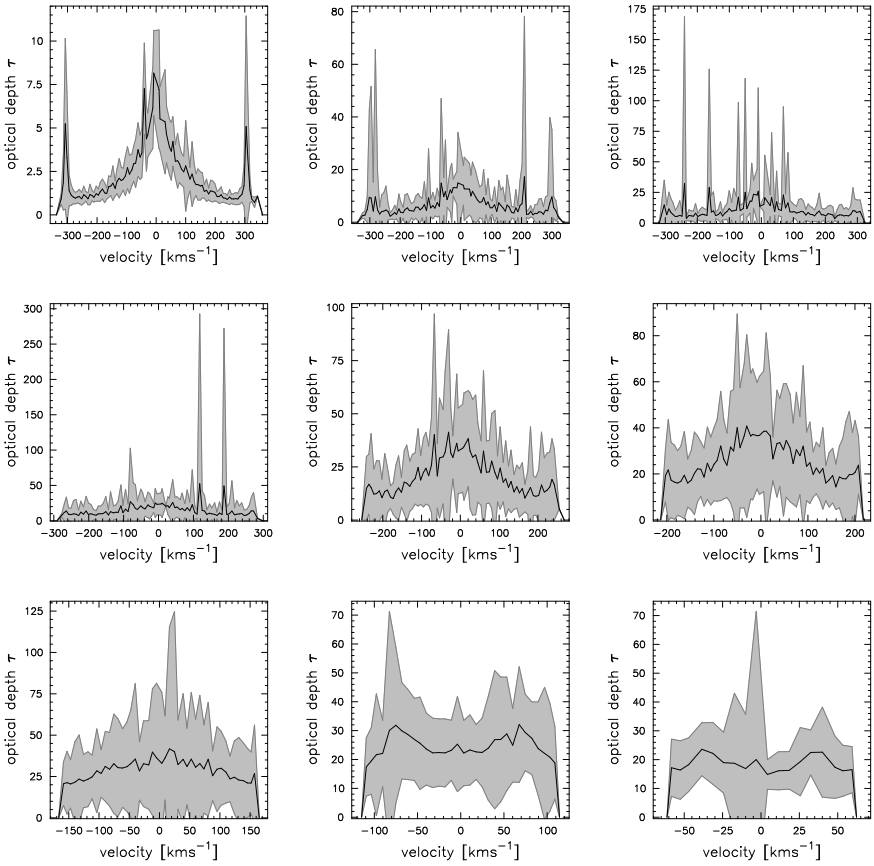

Figure 7.8 – continued; a **truncated disk** geometry seen at different inclinations.

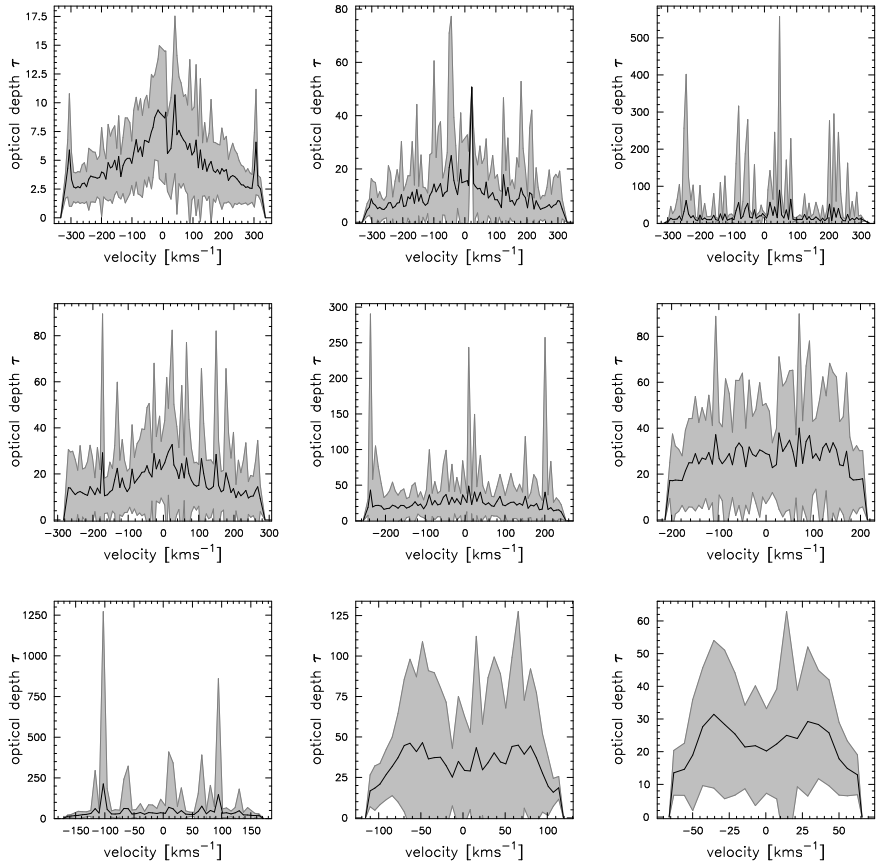

Figure 7.8 – continued; a **disk** geometry seen at different inclinations.

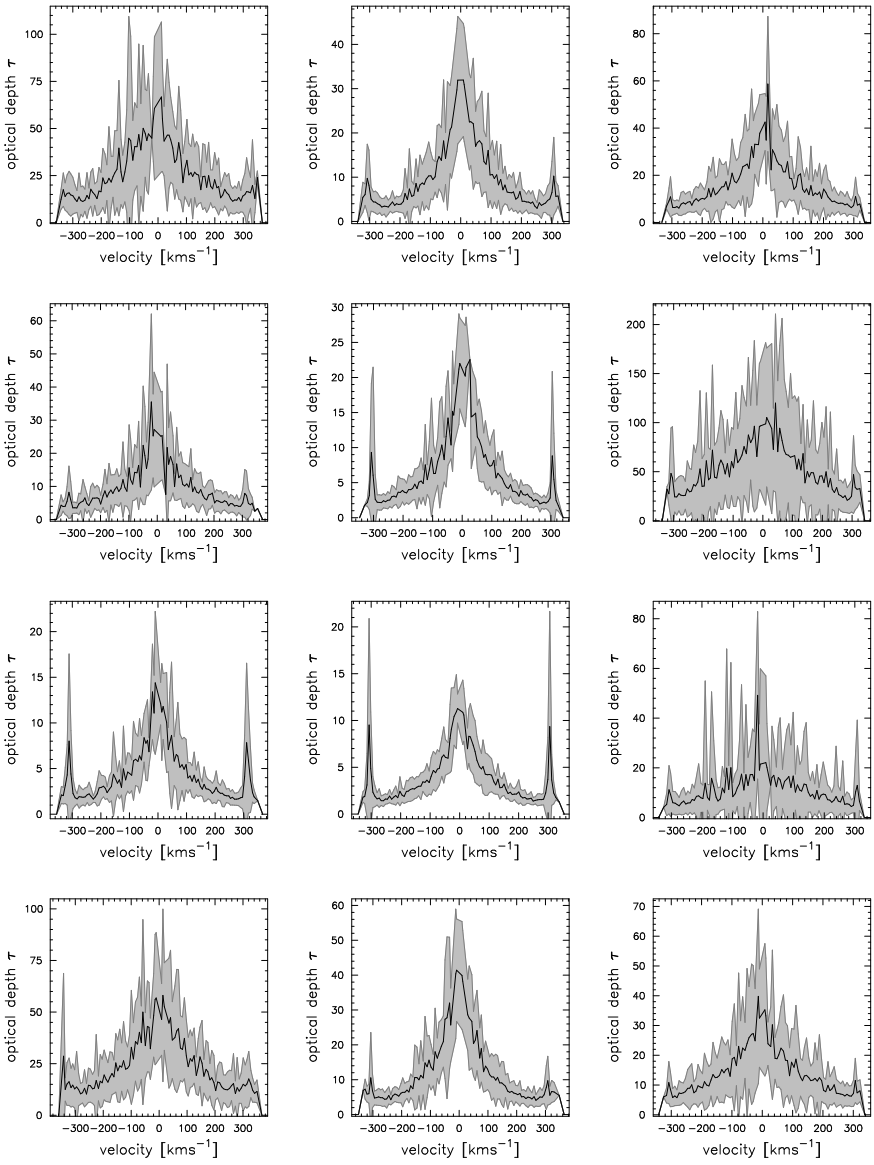

Figure 7.9 – Influence of a background continuum emission on the averaged spectrum. The spectra from left to right are determined for an edge-on **torus**, **truncated disk** and **disk**-geometry. The continuum emission of the different geometries radially affects the individual maser clouds. The spectra from top to bottom show the effect of continuum emission affecting clouds at radial distances of 75%, 50%, 25% and 75% – 25% of the tube diameter of the torus geometry. Each spectrum has a velocity resolution of about 7 $\mathrm{km\,s^{-1}}$ and the estimated error for each velocity bin is indicated by the gray frame.

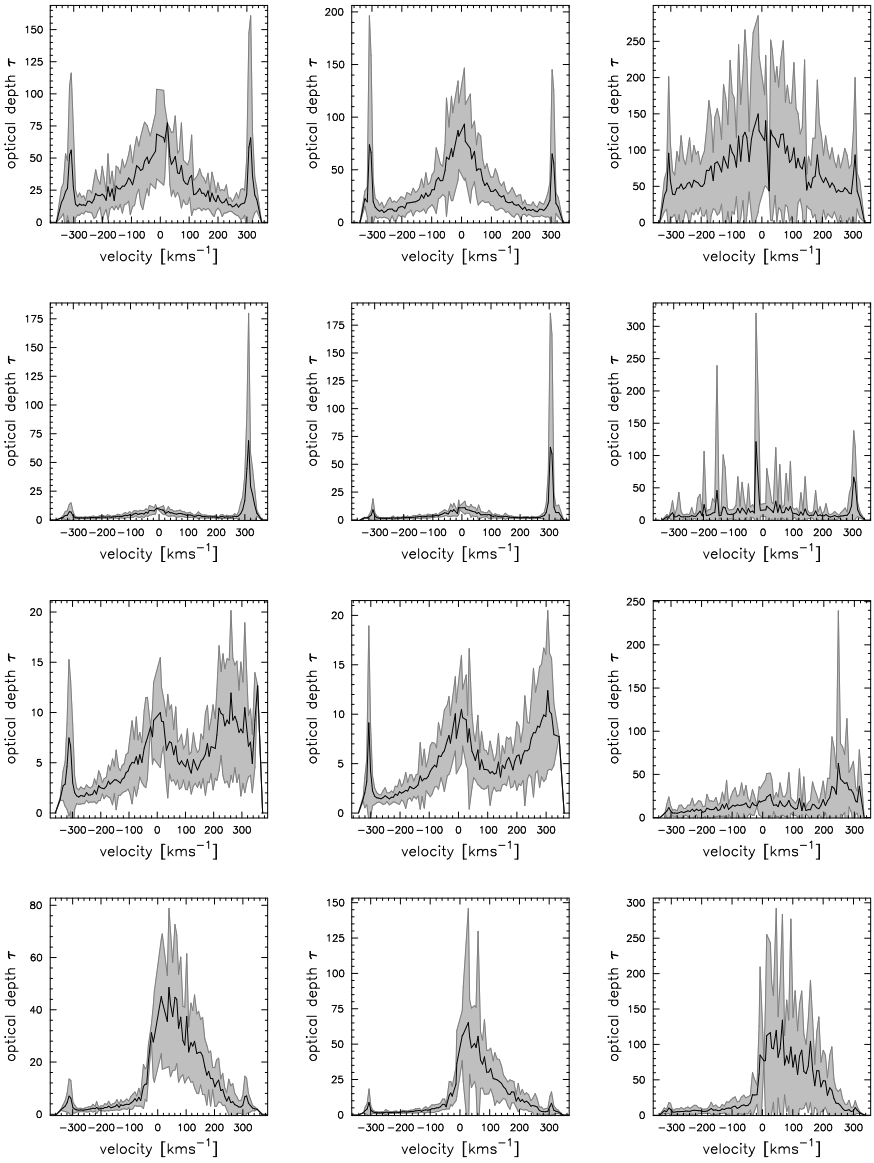

Figure 7.10 – Influence of continuum emission affecting different sections to the averaged spectrum. The spectra from left to right are determined for an edge-on **torus**, **truncated disk** and **disk**-geometry. The ranges of the geometric structure where the continuum emission affects the emissivity of the maser clouds are from top to bottom 180°– 360° (front of each geometry), 180°– 210° (section from 15:00 – 16:00 or 20:00 – 21:00 hrs), 210°– 240° (section from 16:00 – 17:00 or 19:00 – 20:00 hrs), and 240°– 270° (section from 17:00 – 18:00 or 18:00 – 19:00 hrs). Each spectrum has a velocity resolution of about 7 km s^{-1} and the estimated error for each velocity bin is indicated by the gray frame. For visual comparison with spectra not being affected by continuum emission, the spectra at the bottom panel of figure 7.7 may be used.

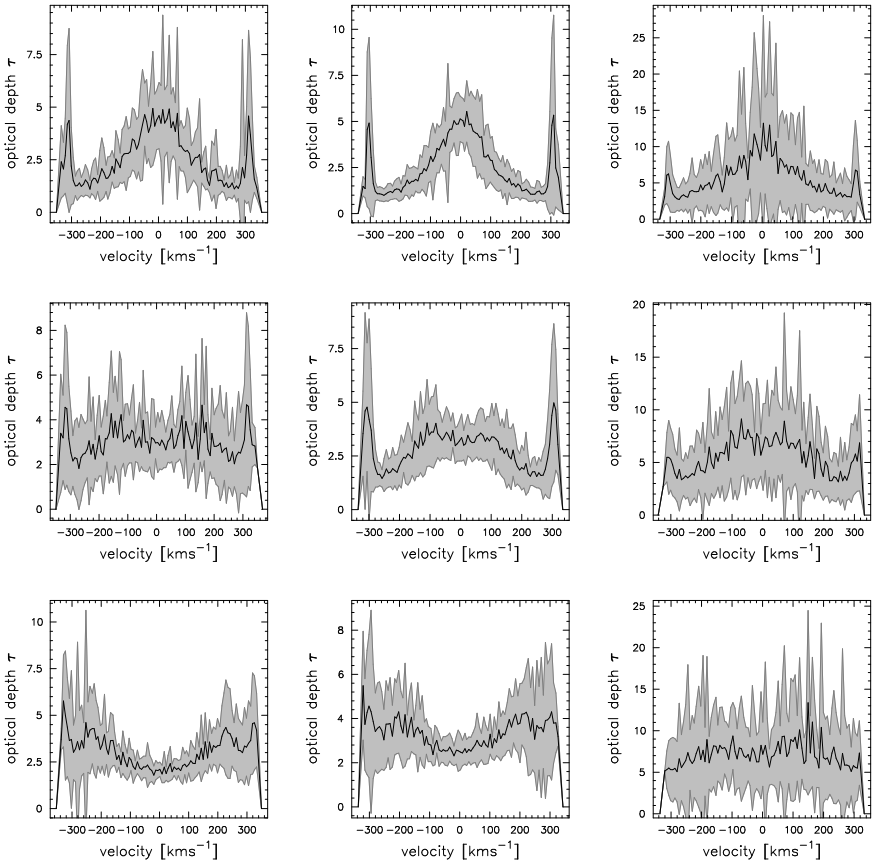

Figure 7.11 – Influence of outflow on the averaged spectrum. The spectra from left to right are determined for an edge-on **torus**, **truncated disk** and **disk**-geometry. The specific outflow will change the orientation of the minor axis of the velocity field. Starting at 15° at the top, the orientation of the minor axis decreases by a step of 15° to the bottom. Each spectrum has a velocity resolution of about 7 km s^{-1} and the estimated error for each velocity bin is indicated by the gray frame. Note that for the disk geometry the regions with low density affect the spectral signature. For visual comparison with spectra not being affected by continuum emission, the spectra at the bottom panel of figure 7.7 may be used.

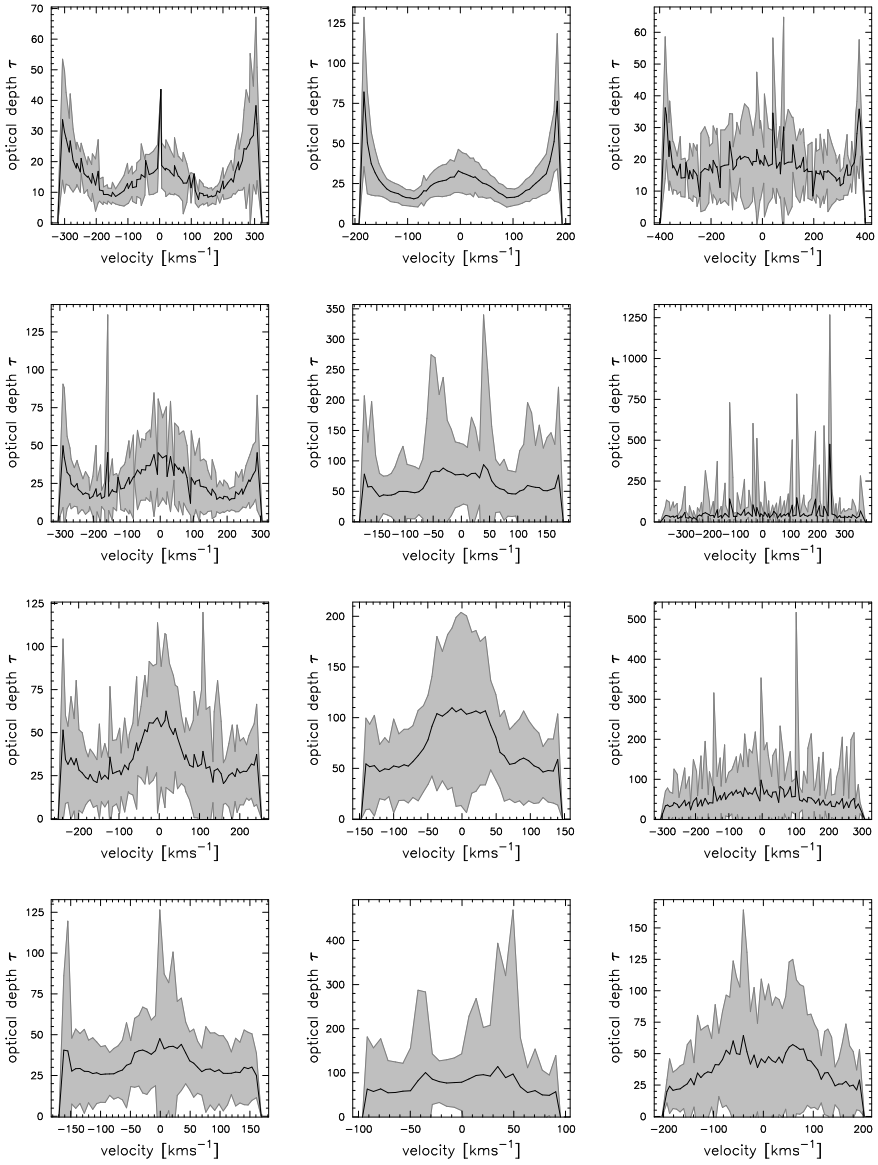

Figure 7.12 – Averaged spectra for solid body velocity field, from left to right, edge-on **torus**, **truncated disk** and **disk**-geometry. From top to bottom the inclination changes from 90° to 30 ° by a step of 20°. Each spectrum has been averaged to a velocity resolution of about 7 $\mathrm{km\,s^{-1}}$ and the estimated error for each velocity bin has been determined by 100 independent cloud distribution and is indicated by the gray frame. The model setup is similar to the parameters used in figure 7.3.